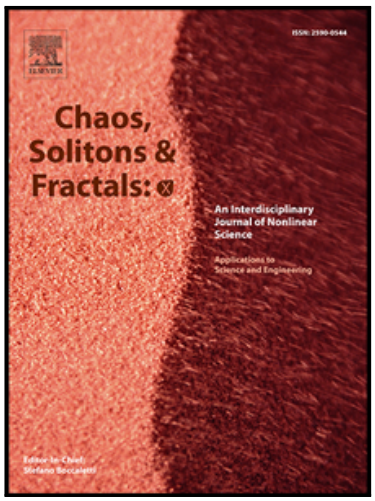

Buildup of Different Emission Regimes in a Nonlinear Polarization Rotation Modelocked All-Fiber Laser

C. CUADRADO-LABORDE , L. TENDELA , E. SILVESTRE , A. DÍEZ , J.L. CRUZ , M.V. ANDRÉS

PII: S2590-0544(24)00011-3
DOI: https://doi.org/10.1016/j.csfx.2024.100114
Reference: CSFX 100114

To appear in: *Chaos, Solitons & Fractals: X*

Received date: 7 April 2024
Revised date: 19 May 2024
Accepted date: 3 June 2024

Please cite this article as: C. CUADRADO-LABORDE , L. TENDELA , E. SILVESTRE , A. DÍEZ , J.L. CRUZ , M.V. ANDRÉS , Buildup of Different Emission Regimes in a Nonlinear Polarization Rotation Modelocked All-Fiber Laser, *Chaos, Solitons & Fractals: X* (2024), doi: https://doi.org/10.1016/j.csfx.2024.100114

Highlights for “Buildup of Different Emission Regimes in a Nonlinear Polarization Rotation Modelocked All-Fiber Laser” by C. Cuadrado-Laborde et al.

- Study of the buildup of light pulses in an all-fiber modelocked laser
- Experimental results were confirmed by numerical simulations
- Determination of the round-trips required to achieve a stable emission state
- Instantaneous angular frequency transient dynamics measurement

Buildup of Different Emission Regimes in a Nonlinear Polarization Rotation Modelocked All-Fiber Laser

C. CUADRADO-LABORDE [1, 2, *], L. TENDELA [1], E. SILVESTRE [3], A. DÍEZ [4], J.L. CRUZ [4], AND M.V. ANDRÉS [4]

1. Instituto de Física Rosario (CONICET-UNR), Blvr. 27 de Febrero 210bis, S2000EZP, Rosario, Argentina,
2. Pontificia Universidad Católica Argentina, Facultad de Química e Ingeniería, Av. Pellegrini 3314, S2002QEO Rosario, Santa Fe, Argentina,
3. Departamento de Óptica, ICMUV, Universidad de Valencia, Dr. Moliner 50, Burjassot E-46100, Spain,
4. Departamento de Física Aplicada, ICMUV, Universidad de Valencia, Dr. Moliner 50, Burjassot E-46100, Spain,
** christiancuadrado@uca.edu.ar*

Abstract: We investigated experimentally and theoretically the buildup of light pulses in an erbium-doped sub-MHz all-fiber laser modelocked by nonlinear polarization rotation. We were able to study the buildup of two different emission regimes: standard solitons and noise-like pulses. In each case, we were able to determine the round-trips required to achieve a stable emission state. Temporal traces and optical spectra of single pulses were measured along the start-up transient of the laser. The experimental results were also confirmed by numerical simulations. Under the specific conditions of this laser, the soliton regime takes about 400 round-trips to reach single-pulse emission. In the noise-like pulse regime, it takes only 20 round-trips for the characteristics of noise-like pulses to show up; although a more steady-state emission is reached also at about 400 round-trips.

Keywords: Fiber lasers, buildup, mode-locking, transient dynamics

1. Introduction

Multiple cavity modes can lock together in a phenomenon known as mode-locking to create a brief pulse of light [1]. From a time-domain point of view, one could say that the laser emits short light pulses produced by a synchronous modulation of the light propagating in the cavity every round-trip. The process typically begins with a narrowband state of quasi-continuous emission in passively modelocked lasers. However, the dynamics of the resonator, in which a strong fluctuation can spontaneously trigger the transition to mode coupling, favor the emission of brief light pulses. It is customary to study this complex phenomenon at steady state, or when the system has reached equilibrium. On the other hand, in order to fully comprehend a specific system, transient dynamics, or the pattern of changes in the system before equilibrium is reached must be studied. However, the lack of high-speed optical spectrum analyzers made experimental observation of these transient dynamics in the Fourier domain fundamentally imprecise [2, 3]. This is due to the fact that a traditional spectrometer, which consists of a grating and an inline sensor, is unable to capture the spectral behavior from noise to stable mode coupling because it develops much faster. But the development of the dispersive Fourier transform method (DFT) opened up new avenues for investigating extremely fast, nonrepetitive events in the optical Fourier domain [4]. DFT maps the spectrum of an optical pulse to a temporal waveform whose intensity can be observed in real time with an oscilloscope using chromatic dispersion produced by either an optical fiber or a grating.

Since then, a number of papers have been presented that monitor both the temporal waveform and DFT to examine the transient dynamics of mode-locking in a few fiber lasers.

Different research teams soon began to investigate the buildup mechanism of the various emission regimes. Herink et al. [5] were the first to use DFT to reveal the transient dynamics of a modelocked laser, as far as we know. They experimentally recorded the spectral evolution of a femtosecond pulse train from round-trip to round-trip in a commercial modelocked free-space laser with a Ti:sapphire Kerr lens. Gao et al. also investigated the probabilistic nature of the state of polarization distributions in the buildup dynamics of dissipative solitons for a net-normal fiber ring laser modelocked by a saturable absorber made of single-walled carbon nanotubes [6]. Using the same resonator, the same authors experimentally observed transient pair formation during the buildup process of dissipative solitons for pump powers greater than those required for stable emission [7]. Chen et al. [8] investigated essentially the same resonator and demonstrated that the appearance of sharp spectral peaks with oscillatory structures during the mode-locking transition is caused by the formation of structural dissipative solitons, validating their experimental results with numerical simulations. Ryczkowski et al. investigated dissipative solitons experimentally in a Fabry-Perot erbium-doped fiber laser modelocked with a SESAM [9]. They characterized the spectral and temporal evolution of ultrashort dissipative solitons as their dynamics undergo an unstable transition state with complex breakup and collisions prior to stabilization using DFT in conjunction with time lensing measurements. It is worth noting that in this case; additional insight was gained by reconstructing the soliton's amplitude and phase and calculating the corresponding complex-valued spectrum. Zhao et al. investigated the dynamics of dissipative soliton buildup in a recently developed all-polarization-maintaining ytterbium-doped fiber laser modelocked by nonlinear polarization evolution in Ref. [10]. Cui and Liu, on the other hand, were able to measure the buildup of conventional solitons, stretched pulses, and dissipative solitons in a fiber laser modelocked by a saturable single-walled carbon nanotube absorber by simply modifying the intracavity dispersion map [11]. Lyu et al. investigated the splitting and motion of dissipative soliton resonance light pulses (DSR) in a ytterbium-doped normal dispersion fiber laser modelocked by a nonlinear optical loop mirror in Ref. [12]. They discovered using the scalar nonlinear Ginzburg-Landau equation that for certain system parameter values, the initial single Gaussian pulse can evolve into an unstable DSR pulse with multiple dark solitons. The coexistence of soliton singlets and molecules in an all-fiber laser modelocked by a 45° tilted fiber grating was also reported by Luo et al. [13]. They discovered that in a cavity with different compositional forms, soliton singlets and soliton molecules coexist. They later used DFT to characterize the vibrational dynamics of soliton triplet formation in a nonlinear polarization rotation fiber laser [14]. The same technique was used by Hamdi et al. to reveal ultrafast dynamics in a passively modelocked thulium-doped fiber laser [15]. In Ref. [16] it is also investigated the dynamics of soliton molecules experimentally. Finally, Woodward and Kelleher demonstrated the existence of slowly decaying dark solitons in the radiation buildup dynamics of bright pulses in all-normal dispersion (ANDI) modelocked fiber lasers by numerically solving the generalized nonlinear Schrödinger equation [17].

In this study, we looked into the development of the different emission regimes found in an all-fiber laser operating at a sub-MHz repetition rate with nonlinear polarization rotation (NPR) as mode-locking mechanism. We selected this laser design in order to benefit from a steady-state characterization we had already completed [18]. By adjusting the pump power and polarization controllers, we found that only two distinct emission regimes—solitons-like pulses and noise-like pulses—can be generated. We were able to register the transient dynamics in each regime in both the temporal and optical frequency domains (via DFT). Furthermore, as far as we are aware, this is the first instance in which it is possible to retrieve the instantaneous angular frequency (or phase, via numerical integration) while a regime of emissions is being created in a modelocked fiber laser. Additionally, we were also able to

compare the outcomes of the numerical simulations we conducted using the scalar nonlinear Schrödinger equation with our experimental findings.

2. Experimental

The laser assembly and the experimental method used to record the various build-up emission regimes are first described in Section 2.1 of the text that follows. We will then present and discuss the various measurements for each build-up emission regime in Section 2.2.

2.1. Set-up

Figure 1 schematically depicts the passively modelocked fiber ring laser's setup. A 2.5 m long, single-clad, erbium-doped optical fiber (EDF) with a numerical aperture of 0.23 and peak absorption of 36.53 dB/m at 1570 nm was used to provide the gain. A 978 nm pigtailed laser diode with a maximum pump power of 600 mW was used to pump the EDF through a 980/1550 nm wavelength division multiplexer (WDM). It is important to note that the output power of this pump laser can be manually adjusted or controlled by an external voltage source. The 90% port of a 90/10 fiber coupler was next connected to the EDF in the counterclockwise direction. The output port of a polarization-dependent optical isolator (PDOI) (PM 1550 panda fiber, fast axis blocked, two-stage, center wavelength 1550 nm, extinction ratio 28 dB) was connected to the input port of the fiber coupler. The input port of the PDOI was next connected to a 210 m long fiber optic delay line (Corning® LEAF®, numerical aperture 0.14, dispersion parameter 6 ps/nmkm). The remaining port of the fiber delay line was then joined to the 1550 nm port of the WDM, successfully closing the cavity. Two fiber optic paddle polarization controllers (PC) were also installed, one before and one after the PDOI, creating a nonlinear polarization rotation NPR saturable absorber. From the 10% port of the optical coupler, this laser's output is obtained. A real-time oscilloscope with fast photodetectors (5 GHz) operating at 2.5 GHz was used to track the light pulses. One of the 50% outputs from the second 50/50 fiber optic coupler—used to split the 10% laser output—was directly recorded by the oscilloscope (channel 1 in Fig. 1), providing the temporal waveform data. For the DFT (channel 2 in Fig. 1), the second 50% output of the fiber coupler was once more transmitted through a 20 km SMF-28 fiber optic coil (dispersive line, DL). This DL is considerable shorter if the instantaneous angular frequency (IAF) profile is measured (100 m of SMF-28 fiber). The signal wave generator (SWG, rise time 8 ns) generated a square wave signal that activated the pump laser. Fig. 1 shows how this signal was applied to properly trigger the oscilloscope. On the other hand, our oscilloscope's highest sampling rate was 2×10^{10} samples/s, which when combined with its maximum memory capacity of 1.025×10^{7} points results in a temporal measurement window of 0.512 ms. The highest temporal resolution that is currently possible can be used to measure 488 round-trips given that this laser has a repetition rate of 949 kHz. Naturally, if the temporal resolution is reduced, the number of round-trips acquired for this particular laser can be increased.

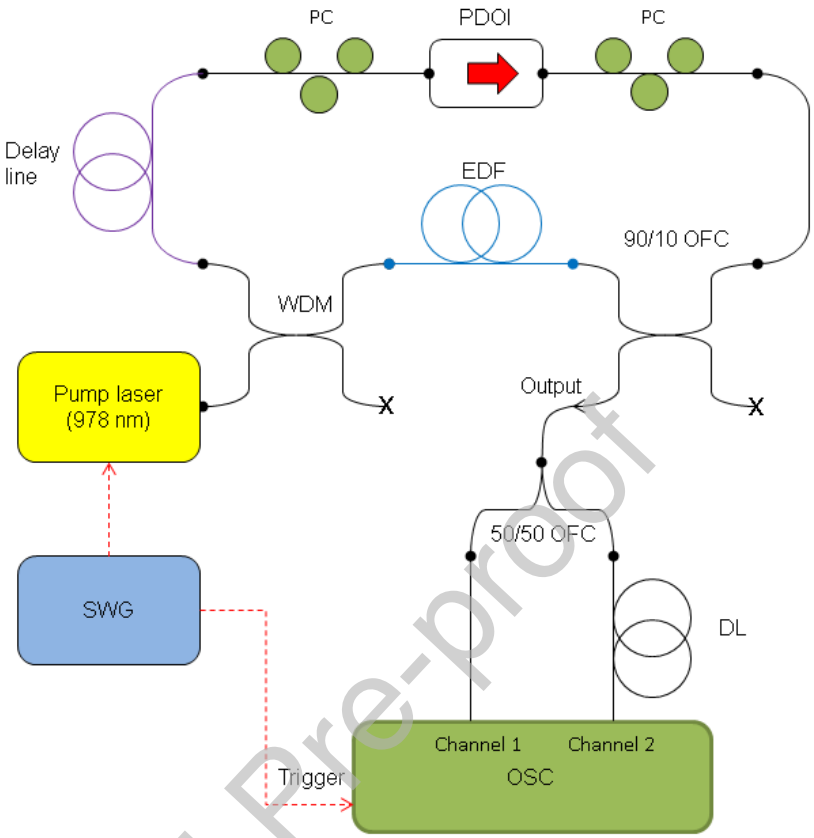

Fig. 1: Experimental setup of the laser, where OSC, SWG, EDF, PC, PDOI, OFC, WDM, and DL stand for: oscilloscope, signal wave generator, erbium doped fiber, polarization controller, polarization dependent optical isolator, optical fiber coupler, wavelength division multiplexer, and dispersive line, respectively.

In this resonator, depending on the position of the polarization controllers and the power of the pump, the interaction of the various components favors different emission regimes, as we have already demonstrated through experimentation. Each regime under study had a similar setup registration procedure that involved the following three steps:

i. The PCs and pump power strength are adjusted manually until the desired regime is achieved.

ii. We turn off the pump power and use the SWG to select the correct square wave voltage to achieve the same pump power that we used in step (*i*). The temporal duration of the square wave voltage applied to the pump unit, on the other hand, should be at least as long as the temporal measurement window (typically > 0.512 ms).

iii. We fed this square wave signal into both the pump power unit and the oscilloscope's trigger input.

We measure the corresponding DFT and the instantaneous angular frequency profile to the temporal waveform of a given round-trip using two different delay lines: 100 m for the instantaneous angular frequency measurement and 20562 m for the DFT measurement, see Fig. 1. In the case of DFT, since the chromatic dispersion is 18 ps / (nm×km) at 1560 nm,

then, resulting in a time-wavelength scaling factor for oscilloscope measurements of 360 ps/nm for a propagation length of 20 km. In the following, we will present and discuss the experimental results for the build-up transient of each emission regime.

2.2. Experimental Results and Discussion

The oscilloscope essentially acquires a single-column data stream with a short-term periodicity determined by the round-trip time *T* of the cavity for both the temporal waveforms and the DFTs. By breaking up the lengthy single-column data into successive intervals of duration *T*, we can transform it into a matrix representation. When appropriate, we will display three-dimensional maps in the text that follows using this matrix data. These maps can be used to represent data in the time or frequency domain (via DFT); the ordinate is the measured normalized intensity, and the abscissas are the round-trip number and a dimensionless time (because it has been divided by the round-trip time). As a result, in this plot, a single and stable pulse emission during a round-trip should produce a straight line. Additionally, it is common to see a slight slope for the ordinate shown in these graphs. This is merely the outcome of this artificial matrix ensemble's interaction with the temporal resolution, and it is of no particular physical interest.

2.2.1. Standard Soliton Regime

We found that this laser exhibits an output of standard soliton-like pulses at steady state when the pump power was set to a moderately low value of 42 mW, while the PC paddles are appropriately positioned. Thus, we applied the procedure described above to track the buildup in this regime. Figures 2a and 2b show the three-dimensional maps for the temporal waveform and DFT, respectively. Apparently, the laser rapidly evolves into a single pulse emission by round-trip, see Fig. 2a. The corresponding DFT soliton track is represented in Fig. 2b and is made up of two quasi-horizontal lines on either side of a central quasi-horizontal stripe. The two Kelly sidebands are represented by these narrow lines, and the soliton spectrum itself is shown by the central stripe. The typical spectrum of interacting solitons [19, 20], however, can be seen by taking a closer look at the corresponding DFT train. This can be seen in Fig. 2b (see the red arrow) as a thin gray stripe starting at round-trip number one and disappearing progressively at round-trip number ~300 at *Time*/*Round-trip time* ≅ 0.003. Additionally, we can see in visualizations 1 and 2; two animations were both the temporal and spectral evolution is shown as the round-trip increases. Of course both visualizations essentially provide the same information shown in Figs. 2a and 2b.

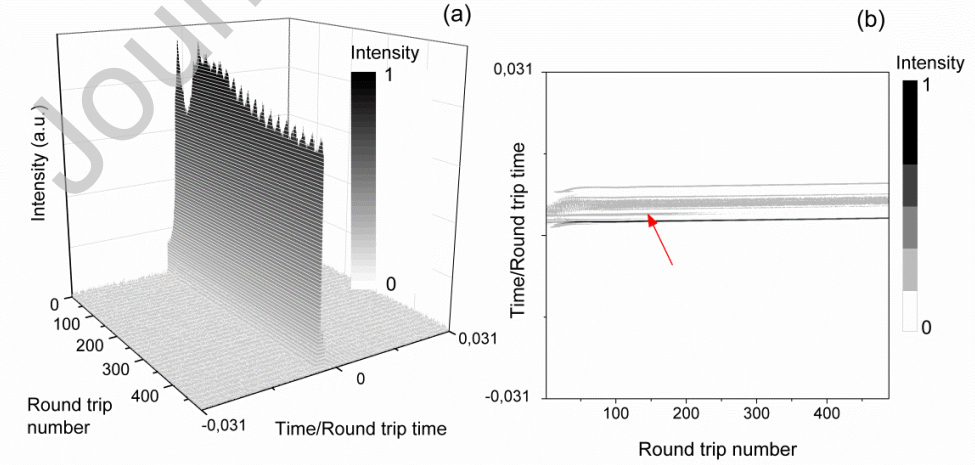

Fig. 2: (a) Experimental build-up in the time-domain (a) and its corresponding DFT for standard soliton-like pulses.

By cutting two lines in Figs. 2a and 2b for round-trip numbers 72 and 460, respectively, we looked into the above details more thoroughly. We compared the temporal waveforms and corresponding DFTs for both round-trips and the results are shown in Figs. 3a and 3c for round-trip 72, and Figs. 3c and 3d for round-trip 460. As can be seen (see Figs. 3a and 3c in comparison to Figs. 3b and 3d), the temporal resolution is insufficient to distinguish between the two (or more) closer solitons in the time domain. Less than 250 round-trips are required to reach the steady-state single soliton-like emission, according to a careful examination of both the temporal waveforms and the DFT trains. The soliton-like pulses that were produced in the steady state had a temporal width of 0.92 ps, an average power of 0.13 mW, and a peak power of 147 W. The measured spectrum, on the other hand, is typically soliton-like, that is, it has spectral sidebands that correspond to dispersive waves, and it has a measured −3 dB bandwidth of 4.66 nm (central wavelength: 1564.3 nm), which is equal to 0.55 THz at the central frequency of 191.64 THz. These soliton-like pulses are therefore roughly transform-limited and have a temporal bandwidth product of TBP = 0.55 THz × 0.92 ps = 0.5 [18].

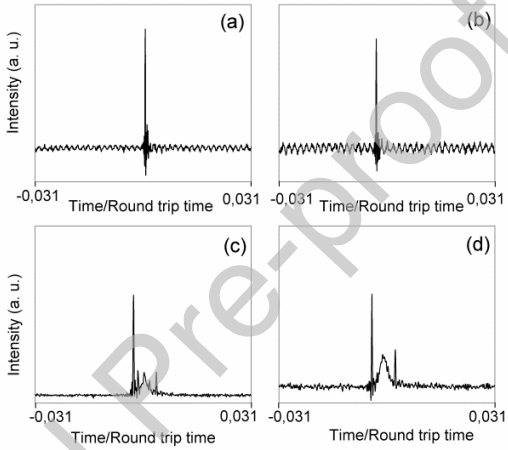

Fig. 3: Soliton-like regime: temporal waveforms and their corresponding DFTs for the 72nd, (a), and (c), and 460th round-trips, (b), and (d), respectively.

2.2.2. Noise-like Pulse Regime

The PCs were then moved while the pump power was increased to create a different emission regime. As a result, we obtain an NLP emission train at 949 kHz with 220 mW of pump power. The transient dynamics of this laser are shown in Fig. 4a. Round-trip 1 marks the start of the sequence, where the pump power enters the cavity. It continues until round-trip 484, where the shot is finished. Figure 4a displays a single emission pulse per round-trip right from the beginning, which is also in line with previous discoveries [21]. Figure 4b shows the radio-frequency spectrum in steady-state NLP mode. The side-lobes around the fundamental frequency help to identify this emission regime.

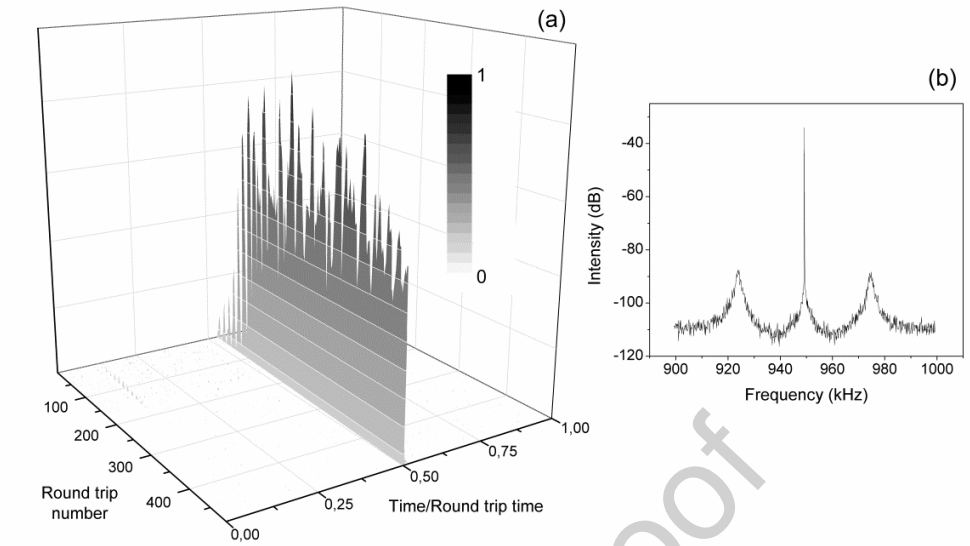

Fig. 4: (a) The build-up of NLPs in the temporal domain. (b) Steady-state radiofrequency spectrum in the NLP regime.

On the other hand, in Fig. 5 we show three cuts from Fig. 4a, representing the temporal waveforms at the 12th, 207th, and 483rd round-trips, where the time window in all cases includes a full round-trip. Under these working conditions, this emission regime reaches a steady-state after the first ~400 round-trips, with a temporal pulse width of 3.7 ns.

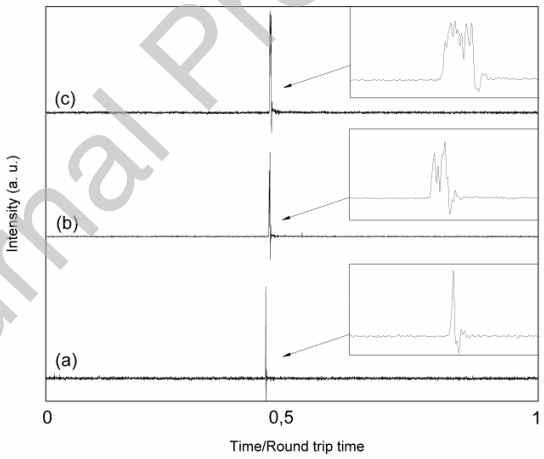

Fig. 5: Temporal waveforms at the 12th (a), 207th (b), and 483rd (c) positions. The zooms to the right are all 30 ns long, while the temporal window lasts for one complete round-trip.

Finally, in Fig. 6 we measured the instantaneous angular frequency profile of the emitted light pulses using a simple technique that we previously developed [22]. The technique requires only the measurement of the temporal intensity waveforms at the input and output of the dispersive line together with the knowledge of the GVD of the optical fiber; then the instantaneous angular frequency profile is obtained only by using a single equation in a non-iterative, one-step numerical calculation. In this case, we show the IAF for the same round-trips as in Fig. 5; i.e., the 12th, 207th, and 483rd round-trips.

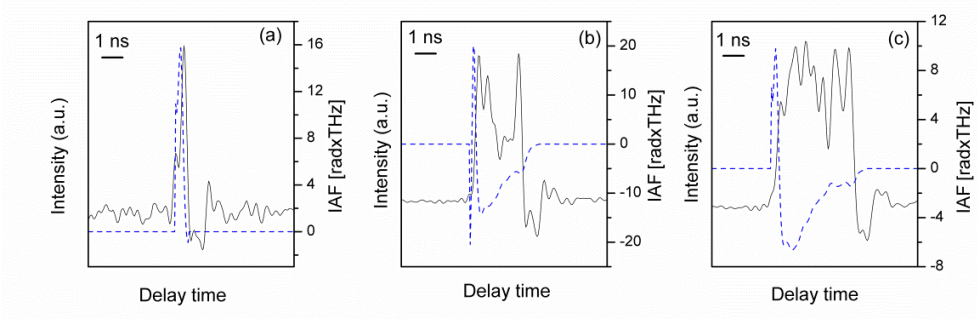

Fig. 6: Temporal waveforms (solid black curve) at the 12th (a), 207th (b), and 483rd (c) round-trips, together with its retrieved instantaneous angular frequency profile (dashed blue curve).

3. Theory and Numerical Results

This section covers the numerical analysis of the laser that was previously examined experimentally in Section 2. In Section 3.1 that follows, the theoretical model is first introduced. The numerical results for each build-up emission regime will then be presented, discussed, and compared with the experimental results in Section 3.2.

3.1. Theoretical Model

The arrangement of the numerical model for this modelocked fiber ring laser is the same as the experimental setup shown in Fig. 1, going clockwise from a gain medium, through a delay line, that produces a nonlinear polarization rotation (NPR), a polarization dependent optical isolator acting as a saturable absorber (SA), and finally an output fiber coupler (OC). The generalized scalar nonlinear Schrödinger equation was used to model the pulse propagation in the cavity [23]:

$$\frac{\partial A}{\partial z} = -\alpha \frac{A}{2} + \int_{-\infty}^{\infty} \frac{g(\omega)}{2} \tilde{A} e^{-j\omega t} d\omega - j\frac{\beta_{20}}{2}\frac{\partial^2 A}{\partial t^2} + j\gamma |A|^2 A \,, \tag{1}$$

where $A = A(z, t)$ denotes the complex envelope of the optical pulse, t is the local pulse time measured in a reference frame moving at the same speed as the signal, z is the propagation distance, α is the linear loss, β_{20} is the second order chromatic dispersion, γ is the nonlinear coefficient, $\tilde{A}$ is the Fourier transform of A, $g(\omega)$ is the gain coefficient; and ω is the baseband angular frequency (i.e., $\omega = \omega_{opt} - \omega_0$, where ω_{opt} is the optical angular frequency and ω_0 is the carrier angular frequency). The gain saturation was considered as

$$g(\omega) = \frac{g_0(\omega)}{1 + \dfrac{\int |A|^2 \, dt}{E_S}} \,, \tag{2}$$

where $g_0(\omega)$ is the gain coefficient for small signals related to the doping concentration having a Gaussian dependence (FWHM bandwidth $\Delta\lambda$), while E_S refers to the saturation energy of the gain, usually related to the pumping strength. Equation 2 represents the gain due to an active medium whose recovery time is much longer than the cavity round-trip time, and therefore does not explicitly depend on time [24]. However, it has been shown that increasing the pumping power increases both g_0 and P_S simultaneously; but keeping g_0 constant and

varying only P_S is usually sufficient to capture the overall dynamic trend [25], so we will follow this procedure from now on.

The saturable absorber results from the action of the NPR combined with the polarizer and the two PCs, one before and one after the PDOI, see Fig. 1. It has been shown that this is equivalent to a Lyot birefringent filter, whose transmission T can be written as [26, 27, 28, 29]:

$$T = \sin^2\alpha\sin^2\beta + \cos^2\alpha\cos^2\beta + \frac{1}{2}\sin 2\alpha\sin 2\beta\cos\left(\Delta\phi_L + \Delta\phi_{NL}\right), \tag{3}$$

where α and β are the angles between the polarization directions of the polarizers and the fast axis of the fiber; $\Delta\phi_L = 2\pi L\Delta n\lambda^{-1}$ and $\Delta\phi_{NL} = 2\pi L n_2 P\cos 2\alpha A_{eff}^{-1}\lambda^{-1}$, are the linear and nonlinear cavity phase delays, respectively, L is the resonator length, Δn is the birefringence, λ is the operating wavelength, n_2 is the nonlinear coefficient, P is the instantaneous power of the input signal, and A_{eff} is the effective fiber core area. From a purely spectral point of view, it is evident that the transmission described by Eq. 3 varies periodically with λ, consequently, it behaves as a spectral comb filter whose channel spacing is given by [30, 31]:

$$\Delta\lambda \simeq \frac{\lambda^2}{L\Delta n}; \tag{4}$$

where L and Δn are the effective length and overall birefringence of the cavity. As a result, the longer the cavity and the stronger the birefringence, the smaller the free-spectral range. Despite the fact that the laser cavity is made of standard single mode fibers, there is some remaining birefringence, plus some extra birefringence due to fiber squeezing in the PCs and fiber winding. Furthermore, the long cavity that we have implies that the nonlinear induced birefringence can dominate over the linear contributions as power is increased. Therefore, not only the spectral spacing and transmission peak position of the intracavity birefringence-induced comb filter can be tuned by rotating the PCs, but also the filtering spectral width, which is half the channel spacing, may change as the pump power is increased [32,33]. The dual dependence of transmission on instantaneous power and optical wavelength can be simplified to single instantaneous power dependence by assuming we are operating at a fixed wavelength within a certain spectral width. As a result, the sinusoidal transmission T of a saturable absorber as a function of instantaneous power P in an NPR is commonly expressed as [34]

$$T = R_0 + \Delta R\sin^2\left(\varphi + \frac{\pi}{2}\frac{P}{P_A}\right), \tag{5}$$

with:

$$\begin{aligned} R_0 &= \sin^2\alpha\sin^2\beta + \cos^2\alpha\cos^2\beta + \frac{1}{2}\sin 2\alpha\sin 2\beta \\ \Delta R &= -\sin 2\alpha\sin 2\beta \\ \varphi &= \Delta\phi_L/2 = \pi L\Delta n\lambda^{-1} \\ P_A &= A_{eff}\lambda/\left(2Ln_2\cos 2\alpha\right) \end{aligned} \tag{6}$$

where R_0 is the minimum transmission, ΔR is the modulation amplitude, φ is the linear phase delay, and P_A is the saturation power for the saturable absorber at $\varphi = 0$, i.e., the peak power at which the pulse reaches a maximum in transmission through the SA. This transmission curve is clearly periodic, with period $2P_A$. The nonlinear contribution can have the same sign

or opposite sign than the linear contribution, depending on the PC angles. Therefore, the range of potential values is: $0 \le R_0 \le 1$, $-1 \le \Delta R \le 1$, $0 \le R_0 + \Delta R \le 1$, and $P_A / P_A^{(min)} \ge 1$, with $P_A^{(min)} = A_{eff}\lambda/(2Ln_2)$. In general, NPR can provide a high modulation depth (up to 100%). Furthermore, in a long resonator NPR fiber laser, P_A (which determines the peak power to obtain maximum transmission) can be relatively low, on the order of a few watts, as we will see later. In the simulations, we will use Eq. 5 for the saturable absorber action of NPR; however, we should keep in mind that the adjustment of the PCs affects not only the parameters related to the saturable absorber action, but also the spectral filtering action.

Table I summarize the numerical parameters that best describe our experimental setup and are invariant with respect to the experimental regimes found above. The model's inherent unidirectionality implicitly accounts for optical isolation. A single round-trip of the simulated laser resonator corresponds to propagation of the signal through all of the model's components. The signal amplitude is reduced by 10% after each round-trip to account for the optical coupler and then re-injected at the start of the program. The numerical simulations were run in a 500-ps time window, with 2^{12} uniformly distributed points, using the split-step Fourier transform method [23]. For each emission regime studied, we used random noise as the initial field, with one photon per frequency channel. In contrast, several papers assume the initial field to be a narrow Gaussian pulse to accelerate convergence, which could be justified in a steady-state analysis. We thought this procedure was much more dubious in our case because we are interested in the build-up of the pulsed emission from the very start.

Table I. Numerical parameters of the optical fibers.

	Parameter	Value	Units
Gain medium EDF	g_0	8.4	m^{-1}
	L	2.5	m
	β_{20}	-7.8×10^{-27}	s^2/m
	γ	4.5×10^{-3}	$W^{-1}m^{-1}$
Delay line LEAF	g_0	0	m^{-1}
	L	210	m
	β_{20}	28.6×10^{-27}	s^2/m
	γ	1.5×10^{-3}	$W^{-1}m^{-1}$

3.2. Simulation Results and Analysis

From the experimental point of view, the only parameters that can be varied to change from one emission region to another are those related to the gain medium and saturable absorption/filtering. The first, via pump power, and the latter, via the change of the positions of the PCs. Therefore, in the numerical simulation, the emission of the different regimes leads to a search in a 6-dimensional space of parameters: E_S, R_0, ΔR, φ, P_A, and $\Delta\lambda$. Where the first parameter, E_S, is related to the pumping strength, while the following five parameters are related to the NPR and SA action, see Eqs. 2-4.

It is interesting to explore which ranges are physically meaningful for the resonator under study. A typically linear birefringence in the cavity is of the order of 2×10^{-6}, which would induce a filtering of ~3 nm bandwidth in a 210 m cavity length at 1562 nm. This value can be taken approximately as the minimum filtering bandwidth; broader bandwidths are easily obtained by assuming a reduced effective linear birefringence, according to Eq. 4. However, in our experiments, the presence of the nonlinear term is obviously the crucial one. On the

other hand, the phase delay, would results in $\varphi \sim 269\times\pi$ rad, but given the known periodicity for trigonometrical functions, essentially results in $\varphi \sim \pi$ rad; we should keep in mind that a slight change in the induced birefringence by the PCs can easily modify this parameter, and the relative sign with respect to the nonlinear contribution. Finally, by assuming $n_2 = 2.7\times10^{-20}$ m^2/W (fused silica), the saturation power is $P_A^{(min)} = 8.9$ W.

3.2.1. Standard Soliton Regime

The standard soliton-like regime was obtained for $E_S = 1.8$ pJ, $R_0 = 0.2$, $\Delta R = 0.05$, $\varphi = 0$, $P_A = 25$ W, and $\Delta\lambda = 20$ nm. Figure 7a depicts the numerically simulated evolution of emission as a function of round-trip number. The cavity initially evolves rapidly in a sequence of multiple solitons per round-trip, up to round-trip number 300, at which point the laser emits a single soliton. Above round-trip number 400, neither the regime nor the laser's pulse properties change. Fig. 7b depicts the time domain waveform in detail; the pulse has an FWHM of 0.97 ps and a peak power of 120 W. The obtained numerical spectrum at round-trip number 1000, with FWHM of 0.55 THz, is shown in Fig. 7c. The spectrum clearly shows the presence of strong sidebands, which is consistent with the steady state measurements. The numerical values in the time and frequency domains agree well with the experimental values described in Section 2.2.1. Furthermore, there is good agreement between the number of round-trips required to obtain a single pulse per round-trip emission in both experimental and numerical results, which are between 300 and 400 round-trips in both cases.

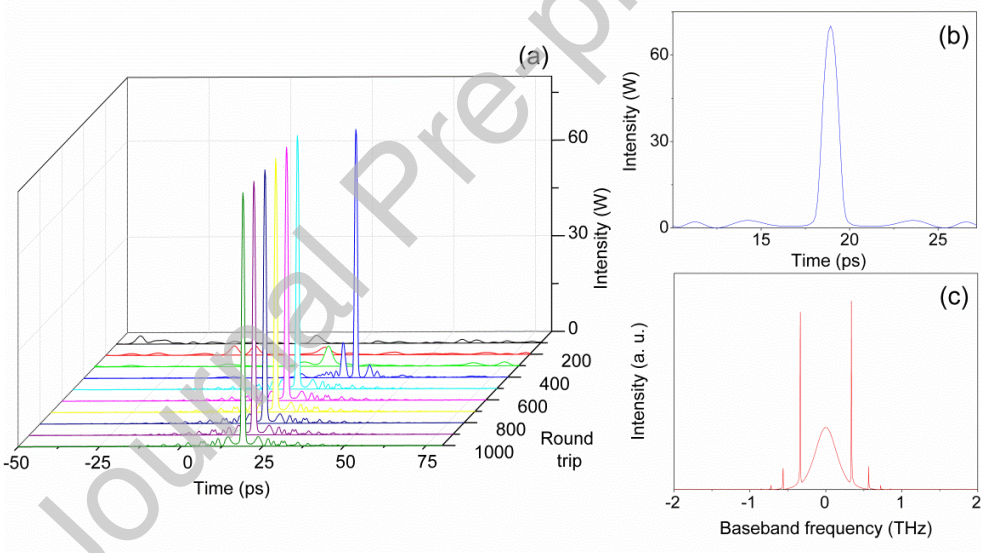

Fig. 7: (a) Time domain build-up for the soliton-like regime, from the first to the thousandth round-trip in one-hundred-round-trip steps. Autocorrelation and spectrum for the thousandth round-trip pulse (b) and (c), respectively.

We discovered that this regime is possible if the filter's bandwidth does not exceed 30 nm. When the filter is narrower than this critical value, the soliton remains roughly unchanged until the filter becomes narrow enough to interfere with the soliton's optical bandwidth, at which point the soliton begins to broaden in time (in this case, below 5 nm). We also found that this regime is extremely sensitive to changes in pump power [35], which can be accounted for by varying E_S in the simulations. This behavior matches our experimental findings for ultra-long soliton lasers, where the pump power must be precisely tuned. It is finally related to the very low repetition rate, because the energy change associated to any change in pump power is spread over a small number of pulses. When E_S is increased by only 8%, two solitons per round-trip appear in the numerical simulations, and so on. By varying the parameters of the saturable absorber, we still can obtain soliton-like emission. The value for

P_A, see Eq. 5, is particularly important; if this value is reduced, the saturation energy of the gain E_S must be decreased as well in order to achieve single soliton-like emission, which is consistent with experimental results. On the contrary, if the saturation energy remains fixed (in this case to E_S = 1.8 pJ), but the saturation power is decreased, single soliton emission practically unchanged is still obtained in the range 5−25 W for P_A. This means the pulse is not affected by the several transmission changes as the peak power rises to 60 W. If the saturation power is reduced further, the pulse will break up into several low peak power pulses. On the contrary, increasing the saturation power completely eliminates the pulsed emission. Finally, if the phase $\varphi = \pi/2$, the pulsed emission is lost completely, or if $\varphi = \pm\pi/4$, two half peak power light pulses are generated, with the remaining parameters held constant.

3.2.2. Noise-like Pulse Regime

The NLP regime was reached for E_S = 60 pJ, R_0 = 0.2, ΔR = 0.8, φ = 0, P_A = 100 W, and $\Delta\lambda$ = 40 nm. Figure 8a depicts the time evolution as a function of the round-trip number. The cavity evolves rapidly in a bunch of pulses in the sequence shown in Fig. 8a. Twenty round-trips are sufficient to produce the typical output of an NLP regime, which is consistent with experimental results; see Fig. 5. Figure 8b shows a numerical autocorrelation performed on the temporal intensity waveform for round-trip number 1000, with the typical NLP autocorrelation spike visible. The numerically determined spectrum is also shown in Figure 8c.

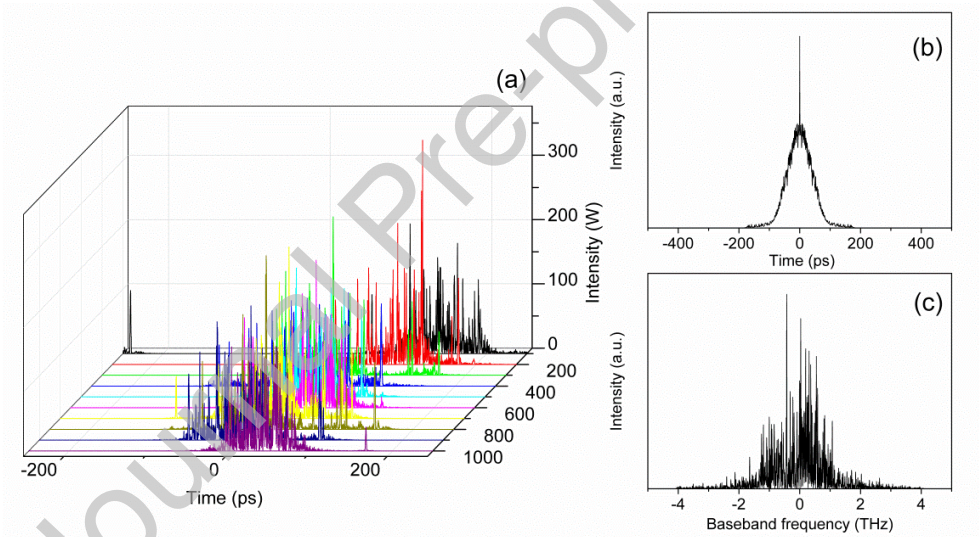

Fig. 8. (a) Time domain build-up for the NLP regime, from the first to the thousandth round-trip in one-hundred-round-trip steps. Autocorrelation and spectrum for the thousandth round-trip pulse (b) and (c), respectively.

We discovered that this regime is independent of the filter bandwidth above a certain threshold; in this case, the NLP regime was obtained above 4 nm bandwidth by fixing the remaining five parameters of the searching space. On the other hand, we observed in our numerical simulation that when the filter bandwidth is narrower, the NLP wave packet is denser, i.e., without the loose pulse peaks shown in Fig. 8a. Otherwise, the general trend remains unchanged.

4. Conclusions

We investigated the experimental buildup of light pulses using an erbium-doped sub-MHz all-fiber laser modelocked by NPR. Our work covers the formation of two distinct emission regimes: soliton-like and noise-like pulses. In each regime, we measured the evolution of both

the temporal traces and the instantaneous spectra, measuring also the instantaneous frequency in the case of noise like pulses. As a result, we determined the number of round-trips required to achieve a single-pulse per round-trip emission. The numerical simulations confirmed the experimental results and provided important information on the ranges in which the parameters could be varied, preserving the emission.

Acknowledgements

This work was supported in part by the European Union, project IPN-Bio (Ref.: H2020-MSCA-RISE-2019-872049), and by the *Generalitat Valenciana* of Spain (Ref.: CIPROM/2022/30).

Disclosures

The authors declare no conflicts of interest.

Data availability statement

Data underlying the results presented in this paper are not publicly available at this time but may be obtained from the authors upon request.

Declaration of interests

☒The authors declare that they have no known competing financial interests or personal relationships that could have appeared to influence the work reported in this paper.

☐The authors declare the following financial interests/personal relationships which may be considered as potential competing interests:

References

1 B.L.N. Binh, N.Q. Ngo, *"Ultra-Fast Fiber Lasers, Principles and Applications"* 1st Ed. CRC Press (2018).

2 Ł. Zinkiewicz, F. Ozimek, and P. Wasylczyk, *"Witnessing the pulse birth—transient dynamics in a passively mode-locked femtosecond laser,"* Laser Phys. Lett. 10, 125003 (2013).

3 J.-C. Kuo and C.-L. Pan, *"Buildup of steady-state subpicosecond and femtosecond pulses in a colliding-pulse mode-locked ring dye laser,"* Opt. Lett. 15, 1297-1299 (1990)

4 K. Goda and B. Jalali *"Dispersive Fourier transformation for fast continuous single-shot measurements"* NaturPhoton 7, 102–112 (2013).

5 G. Herink, B. Jalali, C. Ropers and D.R. Solli *"Resolving the build-up of femtosecond mode-locking with single-shot spectroscopy at 90 MHz frame rate"* Nat. Photon. 10, 321-326 (2016).

6 L. Gao, Y. Cao, S. Wabnitz, H. Ran, L. Kong, Y. Li, W. Huang, L. Huang, D. Feng, and T. Zhu, *"Polarization evolution dynamics of dissipative soliton fiber lasers,"* Photon. Res. 7, 1331-1339 (2019).

7 Y. Cao, L. Gao, S. Wabnitz, H. Ran, L. Kong, T. Zhu, "*Experimental revealing of asynchronous transient-soliton buildup dynamics*," Optics & Laser Technology 133, 106512 (2021).

8 H.-J. Chen, M. Liu, J. Yao, S. Hu, J.-B. He, A.-P. Luo, W.-C. Xu, and Z.-C. Luo, *"Buildup dynamics of dissipative soliton in an ultrafast fiber laser with net-normal dispersion,"* Opt. Express 26, 2972-2982 (2018).

9 P. Ryczkowski, M. Närhi, C. Billet, J.-M. Merolla, G. Genty, and J. M. Dudley, *"Real-time full-field characterization of transient dissipative soliton dynamics in a mode-locked laser,"* Nature Photon 12, 221-227 (2018).

10 H. Zhao, G.-M. Ma, X.-Y. Li, T.-J. Li, H. Cui, M. Liu, A.-P. Luo, Z.-C. Luo, and W.-C. Xu, *"Buildup dynamics in an all-polarization-maintaining Yb-doped fiber laser mode-locked by nonlinear polarization evolution,"* Opt. Express 28, 24550-24559 (2020).

11 Y. Cui and X. Liu, *"Revelation of the birth and extinction dynamics of solitons in SWNT-mode-locked* fiber lasers," Photon. Res. 7, 423-430 (2019).

12 Y. Lyu, C. Wei, W. Du, H. Li and Y. Liu, *"Splitting and Motions of Dissipative Soliton Resonance Pulses in Mode-Locked Fiber Lasers,"* Frontiers in Physics 7, 173 (2019).

13 Y. Luo, Y. Xiang, T. Liu, B. Liu, R. Xia, Z. Yan, X. Tang, D. Liu, Q. Sun, and P.P. Shum, *"Real-time access to the coexistence of soliton singlets and molecules in an all-fiber laser,"* Opt. Lett. 44, 4263-4266 (2019).

14 Y. Luo, R. Xia, P.P. Shum, W. Ni, Y. Liu, H.Q. Lam, Q. Sun, X. Tang, and L. Zhao, *"Real-time dynamics of soliton triplets in fiber lasers,"* Photon. Res. 8, 884-891 (2020).

15 S. Hamdi, A. Coillet, and P. Grelu, *"Real-time characterization of optical soliton molecule dynamics in an ultrafast thulium fiber laser,"* Opt. Lett. 43, 4965-4968 (2018).

16 J. Peng and H. Zeng, *"Dynamics of soliton molecules in a normal-dispersion fiber laser,"* Opt. Lett. 44, 2899-2902 (2019).

17 R.I. Woodward and E.J.R. Kelleher, *"Dark solitons in laser radiation build-up dynamics,"* Phys. Rev. E 93, 032221 (2016).

18 C. Cuadrado-Laborde, J.L. Cruz, A. Díez, and M.V. Andrés, *"Sub-picosecond ultra-low frequency passively mode-locked fiber laser,"* Applied Physics B 122, 273 (2016).

[19] P. Tang, M. Luo, T. Zhao, et al. "*Generation of noise-like pulses and soliton rains in a graphene mode-locked erbium-doped fiber ring laser*," Front. Inform. Tech. El. 22, 303–311 (2021).

[20] J. Li, Z.-J. Yang, S.-M. Zhang, "*Periodic collision theory of multiple cosine-Hermite-Gaussian solitons in Schrödinger equation with nonlocal nonlinearity*," Appl. Math. Lett. 140, 108588 (2023).

[21] C.L. Pan, A Zaytsev, C.H. Lin, Y.J. You, C.H.Wang, "*Progress in short-pulse Yb-doped fiber oscillators and amplifiers*. In: C.C. Lee, Editor. *The current trends of optics and photonics.* Dordrecht: Springer; 61-100 (2015).

[22] C. Cuadrado-Laborde, A. Carrascosa, P. Pérez-Millán, A. Díez, J.L. Cruz, and M.V. Andrés. *"Phase recovery by using optical fiber dispersion,"* Opt. Lett. 39, 598-601 (2014).

[23] G. P. Agrawal, *Nonlinear Fiber Optics*, 4th Ed. (Academic Press, 2007).

[24] G. P. Agrawal, *Applications of Nonlinear Fiber Optics*, 2nd ed. (Academic Press, 2007).

[25] X. Zhang, F. Li, K. Nakkeeran, J. Yuan, Z. Kang, J.N. Kutz, and P.K.A. Wai, *"Impact of Spectral Filtering on Multipulsing Instability in Mode-Locked Fiber Lasers,"* IEEE Journal of Selected Topics in Quantum Electronics 24, 1101309/1-9 (2018).

[26] C.-J. Chen, P.K.A. Wai, and C.R. Menyuk, *"Soliton fiber ring laser,"* Opt. Lett. 17, 417-419 (1992).

[27] W.S. Man, H.Y. Tam, M.S. Demokan, P.K.A. Wai, and D.Y. Tang, "*Mechanism of intrinsic wavelength tuning and sideband asymmetry in a passively mode-locked soliton fiber ring laser*," J. Opt. Soc. Am. B 17, 28-33 (2000)

[28] Z.-C. Luo, A.-P. Luo, W.-C. Xu, et al, *"Tunable multi-wavelength passively mode-locked fiber ring laser using intracavity birefringence-induced comb filter,"* IEEE Photonics Journal 2, 571-577 (2010).

[29] X. Li, S. Zhang, M. Han, and J. Liu, *"Fine-structure oscillations of noise-like pulses induced by amplitude modulation of nonlinear polarization rotation,"* Opt. Lett. 42, 4203-4206 (2017).

[30] H. Lin *et al*., *"Tunable and switchable dual-wavelength dissipative soliton operation of a weak-birefringence all-normal-dispersion Yb-doped fiber laser," IEEE Photonics Journal* 5, 1501807-1501807 (2013).

[31] W. Ma, T. Wang, Y. Zhang, P. Liu, Y. Su, Q. Jia, M. Bi, P. Zhang, and H. Jiang, *"Widely tunable 2 μm continuous-wave and mode-locked fiber laser,"* Appl. Opt. 56, 3342-3346 (2017).

[32] L. Zhao, D. Tang, X. Wu, and H. Zhang, *"Dissipative soliton generation in Yb-fiber laser with an invisible intracavity bandpass filter,"* Opt. Lett. 35, 2756-2758 (2010).

[33] Z.T. Wang, Y. Chen, C.J. Zhao, H. Zhang, and S.C. Wen, "*Switchable dual-wavelength synchronously Q-switched erbium-doped fiber laser based on graphene saturable absorber*," IEEE Photon. J. 4, 869-876 (2012).

[34] Z. Cheng, H. Li, and P. Wang, *"Simulation of generation of dissipative soliton, dissipative soliton resonance and noise-like pulse in Yb-doped mode-locked fiber lasers,"* Opt. Express 23, 5972-5981 (2015).

[35] K. Sulimany, O. Tziperman, Y. Bromberg, and O. Gat, "*Soliton-pair dynamical transition in mode-locked lasers*," Optica 9, 1260-1267 (2022).